CEAS Aeronautical Journal
https://doi.org/10.1007/s13272-026-00947-1

ORIGINAL PAPER

# Investigating and quantifying the ground effect using spectrograms of realistic aircraft flyover measurements

**Anandini Sravya Jayanthi**[1] · **Mirjam Snellen**[1] · **Alireza Amiri-Simkooei**[1]

Received: 4 August 2025 / Revised: 16 January 2026 / Accepted: 30 January 2026


**Abstract**

This paper proposes a measurement-based methodology for investigating the ground effect observed in real-life aircraft flyover measurements in low-noise regions. An acoustic array is used for obtaining a spectrogram of the sound with ground reflections to a large extent eliminated. By applying a model to account for the ground effect, a semi-synthetic spectrogram is obtained. This spectrogram is then qualitatively compared with the spectrogram obtained from single microphone measurements (*Munisense*) at two heights to verify whether indeed the semi-synthetic spectrogram agrees with those measured by corresponding results. As a next step, the ground effect for the flyovers measured is quantified by using the array-recorded signals together with the model for the ground effect for all flyovers. By correcting *Munisense* signals for the estimated ground effect, improved agreement between noise levels at both receiver heights and the array measurements is obtained. Noise differences are evaluated using the proposed alternative metric that only accounts for levels within 4 s duration. For flyovers with higher elevation angles, a greater reduction in noise, up to 2.3 dBA, is observed, despite the larger slant distances. In contrast, flyovers at lower elevation angles show a smaller reduction of approximately 1.8 dBA. This contrasts with the common corrections applied for lateral attenuation in best-practice modeling where the attenuation (accounting for more than only the ground effect) diminishes at higher elevation angles.

**Keywords** ground effect · phased microphone array · flyover measurements · low-noise regions

## 1 Introduction

Over the last decades, the growing public interest in air travel has led to a rapidly increasing number of flights [1]. Although optimizing flight routes and expanding airport infrastructure are straightforward solutions to facilitate this growth, several challenges exist to counteract the adverse effects of this increase. One major concern involves communities affected by aircraft noise around airports. A metric for quantifying the noise exposure is the average Day-Evening-Night noise level ($L_{den}$). According to the World Health Organization (WHO) recommendation, all major European airports must assess noise levels down to a limit of $L_{den} = 45$ dBA [2]. However, regions where $L_{den}$ falls within the 45–55 dBA range are typically classified as low-noise areas and have therefore not been investigated in depth. Studying noise exposure in these regions is important, however, as they cover a larger geographical area and may affect a greater number of people. Consequently, it is essential to accurately assess noise levels in these areas, and ensure that noise prediction models perform reliably even under low-noise conditions. Assessing the models' accuracies can be achieved by utilizing noise data, preferably continuously monitored. In The Netherlands, for example, the so-called Noise Monitoring Stations (NOMOS) have been installed at almost 40 locations around Schiphol Amsterdam airport. Analysis indicates that NOMOS stations situated in low-noise regions record aircraft flyovers over a wider range of lateral distances, altitudes, and elevation angles. The reason is that these regions correspond to stations located outside the fixed take-off and landing corridors. Hence, understanding the propagation phenomenon

✉ Anandini Sravya Jayanthi
a.s.jayanthi@tudelft.nl

Mirjam Snellen
m.snellen@tudelft.nl

Alireza Amiri-Simkooei
A.AmiriSimkooei@tudelft.nl

[1] Operations and Environment, Delft University of Technology, Kluyverweg 1, Delft 2629HS, The Netherlands

Published online: 19 February 2026

affecting the measurements taken in such regions is a key step to undertake before improving the prediction models.

One such model that is investigated in this contribution is a best-practice noise model called the ECAC Doc.29 [3–5]. This model is widely used for monitoring aircraft noise and planning of aircraft operations. It is subjected to a variety of approximations. ECAC Doc.29 relies on the so-called Noise-Power-Distance (NPD) tables, listing the noise level as a function of engine power and distance between the aircraft and the observer [6]. An important approximation is the use of empirical relations to model lateral attenuation as a function of elevation angle and source observer distance [7] to account for propagation effects other than geometrical spreading and atmospheric absorption, since these are already accounted for in the NPD data. The major contributor is the over-ground excess attenuation, which is implicitly attributed to the interference of sound waves due to the presence of the ground, more commonly known as the ground effect. Other effects accounted for in the lateral attenuation are the aircraft directivity and atmospheric propagation effects.

The ground effect arises from the various acoustic propagation paths, arriving at the receiver almost simultaneously. In this contribution we only consider cases with flat ground and no obstacles in the surroundings, resulting in the direct and ground-reflected waves arriving at the receiver [8]. The differences in travel distance for the various paths, and the interaction with the ground result in arrivals that have a relative phase shift. This leads to interference patterns characterized by wave reinforcement and cancellation, often referred to as fringe patterns in the measurements [9]. These interference patterns affect the overall sound pressure levels. Analytical models exist that predict the attenuation or amplification of the sound due to reflection. This phenomenon has been extensively studied under simplified conditions [10, 11], but validation of the predicted attenuation against actual measurements [8] is lacking, a goal addressed in this study. To enable a straightforward analytical calculation of the ground effect, current work is restricted to the assumptions of a homogeneous atmosphere and plane ground surface, as well as a simplified single-ray incidence between the source and the receiver. Under these assumptions, the surface of the ground is characterized by a single parameter (effective flow resistivity) [12] for the grassland. It should be noted that although these assumptions facilitate analytical treatment proposed in this paper, they do not fully capture sound propagation under real-world conditions [11]. Hence, alternative approaches have aimed to characterize ground properties using two parameters [13]. Additionally, the current expressions for lateral attenuation assume no significant attenuation to be present at higher elevation angles (source to observer), $\theta > 50°$. Verifying this through measurements remains a challenge. This is due to the difficulties in uncoupling the ground reflections from acoustic scattering effects at such angles [8]. Therefore, the present study investigates the ground effect across a range of elevation angles to provide insight into improving noise modeling in low-noise regions. This contribution addresses an important element of this research gap by introducing a measurement-based approach that isolates and quantifies the ground effect based on measurements from real-world aircraft flyovers and a straight-forward analytical model. Since measuring the isolated ground effect is a necessary step in the aircraft certification process, several approaches have been studied to measure free-field (without ground effect) noise levels at various points on the flight path. This is generally done by employing a single microphone installed flush-mounted on an acoustically reflective plate. Depending on the position of the microphone on the plate, size, and geometry of the plate. such as the Airbus daisy plate geometry, several approaches have been studied [14–16]. Each of these approaches has significant uncertainties in the measured noise levels due to the edge effects, installation effects and geometrical errors. A thorough investigation of the use of ground-board mounted microphones with different installation methods was carried out by where the variation of sound pressure levels (SPL) on the surface of the ground-board was studied from numerical simulations and measurements in an outdoor environment with a grass-covered field [17].

The goal of this paper is to propose an alternate measuring technique such that these uncertainties are eliminated to a large extent. This is done by the use of a phased microphone-array that is placed on a highly absorbent foam material. The novelty of this work also lies in the use of real-world aircraft flyovers, which is important because it ensures that realistic spectral properties are accounted for.

The measurements considered in this contribution are acquired for a number of aircraft passages in the area around Rotterdam The Hague Airport (RTHA) in The Netherlands. Each real-time flyover measured around Rotterdam The Hague Airport was simultaneously recorded using two single microphones, henceforth called *Munisense*, positioned at different heights, along with a 64-microphone phased array. The trajectory of each of the flyovers is obtained from the Automatic Dependent Surveillance-Broadcast Out (ADS-B) data.

In addition to an increased signal-to-noise ratio, the use of an array also enables source-localization of the aircraft with beamforming. The resulting aircraft locations versus time are compared to ADS-B derived aircraft locations. Time offsets between the acoustic measurements and ADS-B data are resolved by aligning the two location estimates. An additional result from this alignment is a finetuning of the array

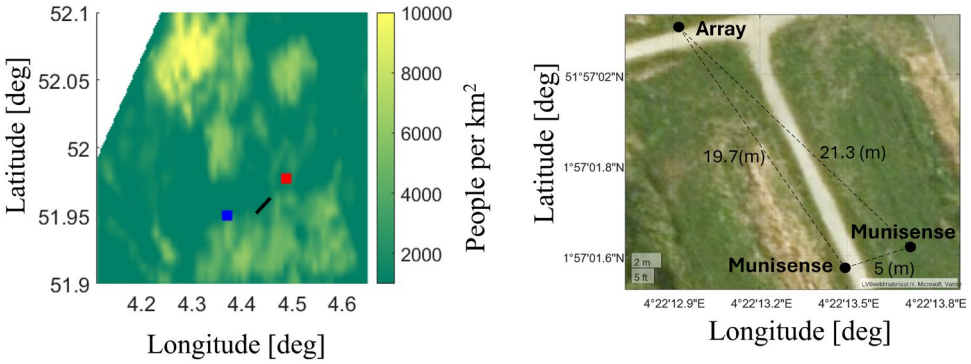


**Fig. 1** Population density map around Rotterdam The Hague Airport (RTHA) showing the runway (black) and the two measurement locations: Location 1 (red) and Location 2 (blue) (left) and the placement of the measurement equipment in the field on Day 3 (right)

**Table 1** Maximum elevation angles and minimum slant distances of flyover measurements conducted near RTHA

| Location | Day | Procedure | Range of $R_{min}$ [m] | Range of $\theta_{max}$ [deg] | Recorded Flyovers |
|---|---|---|---|---|---|
| Location 1 | Day 1 | Arrivals | 250–290 | 39–52.5 | 13 |
| Location 2 | Day 2 | Departures | 595–710 | 49–83 | 8 |
| Location 1 | Day 3 | Arrivals | 270–290 | 38–52.5 | 10 |

orientation. As a next step, data of all microphones is used to capture a spectrogram that is minimally influenced by the ground effect and ambient noise, described as the reference spectrogram in this paper. By applying the analytical model for the ground effect to this reference spectrogram for individual flyovers, semi-synthetic spectrograms are obtained. Each of these semi-synthetic spectrograms has a distinct noise signature, and by comparing it with the corresponding *Munisense* measurements, it is verified that the *Munisense* measurements can be reproduced, thus indicating applicability of the derived semi-synthetic spectrogram. Using the reference spectrogram and the analytical model, the attenuation caused by the ground effect, denoted as $\Delta\mathrm{SPL_G}$, can as such be quantified for any relevant microphone height.

This paper is organized as follows: Sect. 2 describes the measurement dataset and the instrumentation employed in this study. Section 3 outlines the pre-processing steps required for the proposed measurement-based methodology and the applied analytical model. Section 4 details the generation of semi-synthetic spectrograms, along with their qualitative verification, quantification, and subsequent results. Finally, Sect. 5 concludes the paper with a summary of key findings.

## 2 Measurements

This section details the measured aircraft flyovers and the specialized acoustic equipment with which the measurements were made.

### 2.1 Measured flyovers

Aircraft flyovers from Rotterdam The Hague Airport (RTHA) were recorded during measurement campaigns conducted on three separate days in July and August 2024. As shown in Fig. 1, RTHA houses one runway in a moderately populated area, represented by the black line. Measurements were carried out at two locations around the airport: arrivals were captured at Location 1 (red square), and departures were captured at Location 2 (blue square), as indicated in Fig. 1. The maximum grazing angles, also denoted as elevation angles in this contribution, $\theta_{\max}$, and minimum slant distances, $R_{min}$, of the aircraft at their closest point of approach, relative to the observer, are given in Table 1. The flyovers that were recorded exhibit varied trajectories where generally the ones with lower overhead elevation angles occurred on days 1 and 3 and flyovers with higher overhead elevation angles occurred on day 2.

### 2.2 Measurement equipment

Each aircraft flyover was recorded simultaneously by three measurement systems: two single microphones positioned at different receiver heights, and a 64-microphone phased array. These systems were placed close enough to ensure consistent acoustic conditions for each flyover, yet far enough apart to avoid mutual interference, as seen in Fig. 1. These devices offer high sampling frequencies and advanced sound recognition capabilities, which allow real-time audio data to be captured and stored in the cloud. To ensure accurate measurements, each *Munisense* unit is equipped with wind protection, as shown in Fig. 2. In addition to the *Munisense*, each flyover was recorded by a 4 m×4 m phased asymmetric array that consists of 64 MEMS microphones. The microphones have a low sensitivity tolerance to accommodate for the high sound levels near the airport. To minimize the effects of reflections, the array was placed on a damping foam on the ground, and its primarily metallic

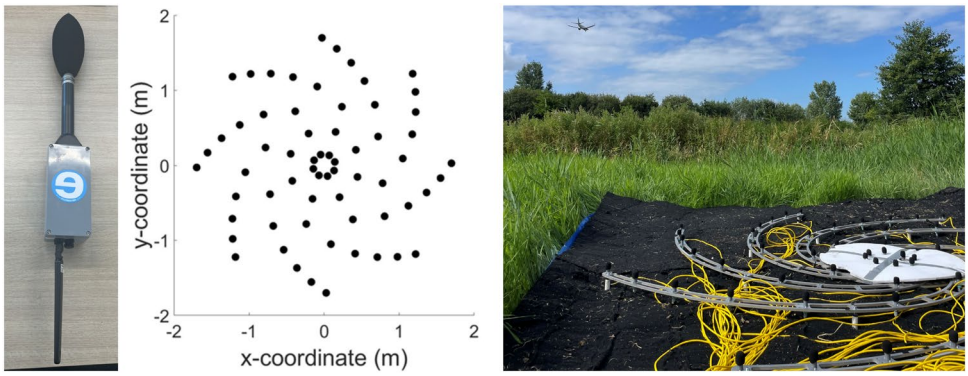


**Fig. 2** Portable *Munisense* with wind shield (left); sketch of a phased asymmetric array with 64 MEMS microphones (middle) and the field measurement setup of the phased asymmetric array with 64 MEMS microphones that are wind protected, with dampening foam installed (right)

**Table 2** Types of measurement equipment with corresponding specifications

| Setup | Specifications | Height [m] | $F_s$ [Hz] |
|---|---|---|---|
| *Munisense* | Portable & Light | 1.75 | 48000 |
| *Munisense* | Portable & Light | 4.5 | 48000 |
| Phased microphone array | Portable & Heavy | 0.08 | 62500 |

**Table 3** Types of absorbing foam installed in the measurement setup with Noise Reduction Coefficient (NRC), thickness and effective frequency range $F$

| Name | Placement | NRC | Thickness [mm] | $F$ [Hz] |
|---|---|---|---|---|
| Akotherm Basic 40/25 [18] | On the ground | 0.6 | 25 | Above 500 |
| Flamex GU [19] | Above the structure | 0.8 | 15 | – |

internal structure was also shielded with an additional acoustic absorbing foam, as seen in Fig. 2. Each of the microphones in that array was covered with wind shields to reduce the interference effects due to wind. The specifications and configuration of the equipment setup are detailed in Table 2 and the details of the foam are mentioned in Table 3. In this paper, it is assumed that all the reflections are fully absorbed.

## 3 Methodology

This section details the preprocessing steps required to ensure an accurate time alignment of individual noise events. It also outlines the process of obtaining a spectrogram with minimal ground effect, referred to as the reference spectrogram. Finally, the approach towards quantifying the ground effect on measured levels is presented.

### 3.1 Preprocessing and time synchronization

In addition to obtaining the reference spectrogram, the microphone array plays a crucial role in aligning the time axis of the various measurement systems. Each flyover is recorded by three setups: two *Munisense* systems, which share the same internal system. With the array as a reference time-axis, the noise event recorded by *Munisense* is manually aligned. Additionally, aircraft positions as a function of immission times, i.e., the time at which the sound wave reaches the array, are calculated by applying a time shift to the emission times for which Automatic Dependent-Surveillance Broadcast (ADS-B Out), data are stored. This is done by employing the relation given in Eq. 1. The time delay between emission $t_e$ and immission $t_i$ of the signal from source to the receiver is given as follows:

$$t_i = t_e + \frac{r}{c}, \tag{1}$$

where $r$ is the distance traveled by the sound from aircraft to the receiver and $c = 340$ m/s is the speed sound in air.

Conventional Frequency Domain Beamforming (CFDBF) [20] is applied to the array data and the acoustically derived aircraft location is obtained in spherical coordinates by finding the maximum in the beamforming output. In the applied CFDBF approach, the aircraft location is obtained from broadband beamforming maps constructed by incoherently averaging the narrow band beamforming results. This was done for a predefined coarse grid with elevation angles ranging from $0:90°$ and azimuthal angles ranging from $0:360°$ with a resolution of $0.01°$. In this work, beamforming maps were computed for frequency bands spanning from 100 to 5100 Hz, using a bandwidth of 100 Hz. Frequencies above 5100 Hz were not considered, as atmospheric attenuation was assumed to significantly limit their contribution to reliable localization. Within each frequency band, beamforming was performed at the steps of 10 Hz and the resulting narrow band beamforming maps were then incoherently averaged within these frequencies. Then, the final aircraft position was determined as the grid point with the maximum response. This was done for many time instances by

dividing the recorded data into 0.15 s snapshots of data without any overlap [21].

Figure 3 illustrates the location of a departing flyover of B737-800 in spherical coordinates, where $\theta$ is the elevation angle and $\phi$ is the azimuthal angle between the source and the observer. In this figure, the acoustically obtained locations (with CFDBF) are denoted by blue dots and the dashed black line represents the original ADS-B trajectory after accounting for the immission time-axis which is calculated as given in Eq. 1. The time offset between the acoustically obtained locations and ADS-B obtained locations time-axis is denoted as $\Delta$T. By accounting for this offset the ADS-B trajectory is aligned with the CFDBF trajectory, denoted as the blocked black line. Initially, the orientation ($\Delta\phi$) of the array was determined using a compass in the field, but, to avoid measurement errors, the orientation was subsequently fine-tuned by aligning the ADS-B locations with those obtaining from CFDBF through incremental steps of $0.25^\circ$ for each measurement on each of the measurement days. In this example, $\Delta T = 65.305$ seconds and $\Delta\phi = 58.2^\circ$. Both the ADS-B derived trajectory and the acoustically derived aircraft trajectory show little jumps, the former due to the pre-processing of ADS-B trajectories that has errors in interpolation due to the absence of data at certain time-stamps, which persist even after applying several filters which are shown in Olive et al [22].

Once aligned, quantifying the ground effect requires a reference spectrogram, with minimal contributions from ground reflections and ambient noise. For each flyover, its corresponding reference spectrogram is obtained, for snapshot lengths of 0.25 s, by calculating the Power Spectral Levels for each microphone (PSL) and averaging them across all microphones in the array. The snapshot lengths selected for beamforming and for determining the PSL differ for two reasons. Firstly, snapshot lengths exceeding 0.15 s lead to irregular source-localization patterns, manifested as an increased number of scattered localizations. This effect is visible in Fig. 3, where several localized points do not align with the ADS-B trajectory. Secondly, a snapshot length of 0.25 s for determining the PSL was selected to ensure alignment of the time axes between the *Munisense* sensors and the array, which is essential for a consistent comparison of the spectrograms obtained from the two measurement systems. The advantage of spatially averaging the PSL can be seen in Fig. 4a and b, where the spatially averaged spectrogram is compared with a single microphone in the array. The doppler-shifted curves of the Blade Passing Frequency (BPF) and its harmonics are seen clearly in the former, thus capturing more spectral information than a single microphone. Additionally, the atmospheric effects such as turbulence due to wind that are observed by all the microphones are implicitly considered while computing the spatial average of the pressure signals of all the microphones in the phased-microphone array. Alternatively, the spectrogram could have been obtained by beamforming the array data; however, the beamformed spectrum shows irregular patterns, as seen in Fig. 4cand the acoustic localizations.

### 3.2 Analytical calculation of the ground effect

Once the flight trajectory is determined and verified, the influence of ground interference is analyzed. As the sound wave propagates from the source to a receiver, it loses energy due to atmospheric absorption and geometrical spreading and potentially scattering. In addition, the ground alters the sound field through constructive and destructive interference, known as the ground effect. At certain frequencies, this results in amplification or attenuation, which forms a characteristic fringe pattern. The

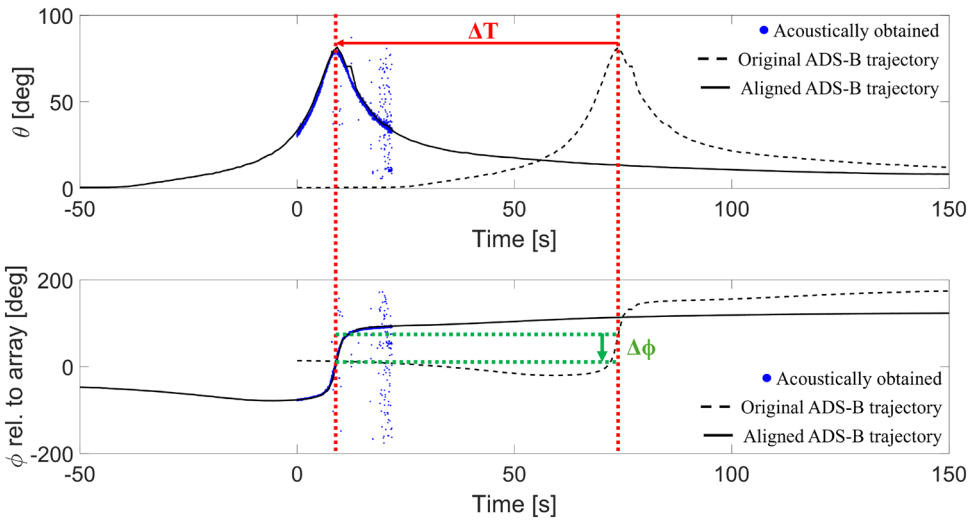


**Fig. 3** Synchronization of time axes by aligning the acoustically obtained locations (blue dots) with the original ADS-B trajectory (dashed black lines) of a B737-800 departing flyover. Here, $\Delta$T denotes the time offset, and $\Delta\phi$ represents the orientation offset of the array. The solid black line shows the ADS-B trajectory after applying both offsets

**Fig. 4** Comparing spectrograms of a B737-800 arrival flyover

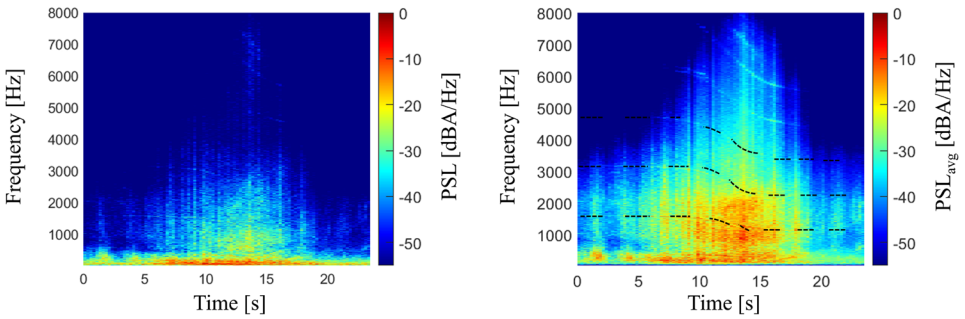


(a) Spectrogram obtained from a single microphone of the phased-microphone array.

(b) Spatially averaged spectrogram with highlighted dashed black lines representing harmonics of the engine fan.

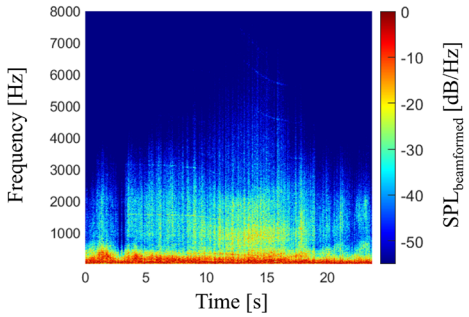


(c) Beamformed spectrogram obtained from all the microphones in the phased-microphone array.

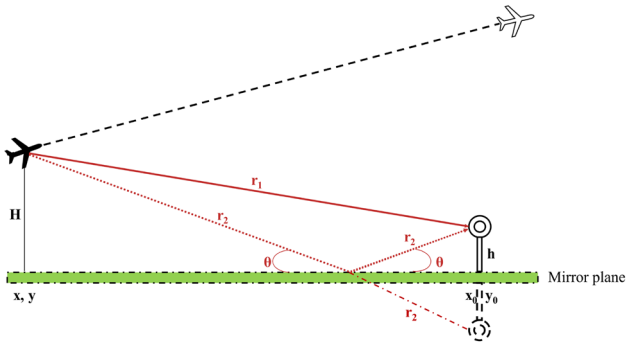


**Fig. 5** Direct and ground-reflected wave paths ($r_1$ and $r_2$) from the aircraft to the microphone position installed at hight $h$

pattern occurs due to the phase shift caused by the interaction with the ground and the difference between the length of the direct path ($r_1$) and ground-reflected path ($r_2$) to the receiver, as illustrated in Fig. 5.

The main input required to synthesize the ground effect is the location of the aircraft relative to the position of the receiver and the properties of the ground. The path lengths of the direct and ground-reflected rays, $r_1$ and $r_2$, are calculated from the verified real-time trajectory of each flyover from the corresponding ADS-B data. For a receiver height $h$, the two ray path lengths and the elevation angles are calculated as follows:

$$r_1 = \sqrt{(x - x_0)^2 + (y - y_0)^2 + (H - h)^2}, \tag{2}$$

$$r_2 = \sqrt{(x - x_0)^2 + (y - y_0)^2 + (H + h)^2}, \tag{3}$$

$$\theta = \arcsin\left(\frac{H - h}{r_1}\right), \tag{4}$$

where $(x, y)$ denote the two horizontal coordinates of the aircraft relative to the receiver position $(x_0, y_0)$, and $H$ represents the aircraft's altitude.

In addition to the source and receiver heights, the characteristics of the ground surface play an crucial role in determining how much sound is reflected, absorbed, or scattered before reaching the observer. While modeling a mixed-impedance ground provides a more realistic representation of outdoor sound propagation, it is computationally expensive [23]. Therefore, in this study, the propagation environment is simplified by assuming a uniform and smooth plane reflecting surface [24]. This terrain is simulated by calculating the normalized surface impedance $Z_n$ over half of the array's sampling

frequency of $f = 31250$ Hz. The calculation is based on the effective flow resistivity of mixed terrain, representative of the terrain where the measurements were taken, $\sigma_e = 250\ \mathrm{kPa/m^2}$ using the empirical power-law model proposed by Delany and Bazley [25],

$$Z_n = 1 + 9.08\left(\frac{\sigma_e}{f}\right)^{0.75} - i11.9\left(\frac{\sigma_e}{f}\right)^{0.73}, \tag{5}$$

with the imaginary unit $i = \sqrt{-1}$. The normalized surface impedance $Z_n$ is further applied to calculate the plane reflection coefficient of the ground

$$Q = \frac{Z_n \sin\theta - 1}{Z_n \sin\theta + 1}. \tag{6}$$

Following the analytical equations described in [24], the overall ground interference effect $\Delta\mathrm{SPL_G}$ in dB is calculated as

$$\begin{aligned}\Delta SPL_G =& 10\log_{10}\left(1 + \left(\frac{r_1^2}{r_2^2}|Q|^2\right)\right.\\ &\left. +2\frac{r_1}{r_2}|Q|\cos\left(\frac{2\pi f}{c}(r_2 - r_1) + \psi\right)\right),\end{aligned} \tag{7}$$

where $|Q|$ is the amplitude of the plane reflection coefficient of the ground and $\psi$ is it's corresponding phase.

Subsequently, using the analytically computed ground effect, $\Delta\mathrm{SPL_G}$ and the spatially averaged levels $\mathrm{PSL_{avg}}$, the influence of the isolated ground effect on audible noise levels, $\Delta\mathrm{L_{A,G}}$ is quantified. This is done by following a series of steps, as detailed in Algorithm 1. Firstly, the reference power spectral levels, $\mathrm{PSL_{ref}}$ are obtained by applying A-weighting to $\mathrm{PSL_{avg}}$ over the relevant frequency range. The reference overall sound pressure levels, $\mathrm{SPL_{ref}}$ and the corresponding A-weighted noise level time series, $\mathrm{L_{A,ref}}$ are then calculated. Secondly, the power spectral level $\mathrm{PSL_G}$ (which is described as the semi-synthetic spectrogram and further explained in Sect. 4) is calculated by superimposing the ground effect on the reference spectrogram, from which the corresponding overall sound pressure levels $\mathrm{SPL_G}$ and A-weighted noise level time series are derived $\mathrm{L_{A,G}}$. Once both the reference time series (without ground effect) and the time series including ground effect have been computed, the former is subtracted from the latter to obtain the difference in noise levels caused purely due to the ground effect as $\Delta\mathrm{L_{A,G}}$. Finally, this isolated ground-effect contribution calculated from the array microphones will be applied to the *Munisense*-measured overall A-weighted noise levels to derive the corresponding free-field noise levels. This procedure will be carried out for the two receiver heights.

**Require:** Spatially averaged power spectral levels as a function of time averaged over all microphones: $\mathrm{PSL_{avg}}$
**Require:** Correction for A-weighting with the frequency range of the array: dLA
**Require:** Frequency resolution: $\Delta f$
**Require:** Ground effect correction at the receiver height according to Equation 7: $\Delta\mathrm{SPL_G}$

1: Correct the averaged power spectral levels as a function of time averaged over all microphones for A-weighting:

$$\mathrm{PSL_{ref}}(f) = \mathrm{PSL_{avg}}(f) + \mathrm{dLA}(f)$$

2: Compute the sound pressure level (SPL) from power spectral levels with correction for A-weighting as measured by the array in $\Delta f$ bands (3.25 Hz):

$$\mathrm{SPL_{ref}}(f) = \mathrm{PSL_{ref}}(f) + 10\cdot\log_{10}(\Delta f)$$

3: Compute the Overall A-weighted Sound Pressure levels of the reference spectrogram by summing it over all the frequency bands, $n$:

$$\mathrm{L_A} = 10\log_{10}\left(\sum_{i=1}^{n} 10^{\frac{\mathrm{SPL_{ref}}(f_i)}{10}}\right)$$

4: Compute the A-weighting corrected power spectral levels of semi-synthetic spectrogram:

$$\mathrm{PSL_G}(f) = \mathrm{PSL_{ref}}(f) + \Delta\mathrm{SPL_G}$$

5: Compute the sound pressure level (SPL) from semi-synthetic(superimposed) power spectral levels:

$$\mathrm{SPL_G}(f) = \mathrm{PSL_G}(f) + 10\log_{10}(\Delta f)$$

6: Compute the Overall A-weighted Sound Pressure levels of superimposed spectrogram by summing it over all the frequency bands, $n$:

$$\mathrm{L_{A,G}} = 10\log_{10}\left(\sum_{i=1}^{n} 10^{\frac{\mathrm{SPL_G}(f_i)}{10}}\right)$$

7: Compute the difference between the reference and superimposed Overall A-weighted Sound Pressure levels for all snapshots considered:

$$\Delta\mathrm{L_{A,G}} = \mathrm{L_{A,G}} - \mathrm{L_A}$$

**Algorithm 1** Influence of ground effect on overall A-weighted sound pressure levels calculated using the phased-microphone array

## 4 Results

This section demonstrates the methodology described in the previous section to obtain a semi-synthetic spectrogram, i.e., with the spectrogram derived from the array data, corrected for ground effects as predicted by the analytical model. The validity of these semi-synthetic spectrograms is investigated by visually comparing them with the *Munisense* measured spectrograms at two receiver heights. Once a qualitative match is achieved, the level differences $\Delta\mathrm{L_{A,G}}$ are calculated. Finally, a comparison of all flyovers is performed for both receiver heights with and without correction for the ground effect on the array-measured spectrograms.

### 4.1 Semi-synthetic spectrogram

For each noise event, the reference spectrogram $\mathrm{PSL_{ref}}$ (A-weighted) was generated by spatially averaging the acoustic intensity across all functional microphones in the array for a snapshot length of 0.25 s across the entire

duration of the event. The representative example corresponding to the arrival of a B737-800 that was shown in Sect. 3.1 is continued here. Figure 6a shows the reference spectrogram, limited to frequencies between 0-1000 Hz, since interference-related fringes are clearly distinguished within this range. Then the analytically calculated ground effect for a receiver height of 4.5 m is presented in Fig. 6b. The calculated ground effect was subsequently superimposed on the reference spectrogram, to produce the semi-synthetic spectrogram illustrated in Fig. 6c. This figure shows the amplification caused by the ground effect in white and the attenuation is shown in gray. Additionally, an arbitrary threshold of 21 dBA below the maximum value of $\mathrm{PSL_G}$ is chosen to highlight the amplified fringes.

## 4.2 Qualitative verification and quantification

The verification of the semi-synthetic spectrograms is done by comparing them with the corresponding *Munisense* measured spectrograms. Figure 7 and Fig. 8 present the verification of the same exemplary flyover presented above. These figures show the superimposed semi-synthetic spectrograms alongside the *Munisense*-measured spectrogram at receiver heights of 1.75 m and 4.5 m, respectively. Key characteristics such as the number of interference fringes, their frequency band coverage, and the snapshot at which the dip occurs are visually compared, which demonstrate a good qualitative agreement.

Once this agreement is established, the influence of the ground effect on overall noise levels, quantified as $\Delta \mathrm{L_{A,G}}$, is computed as explained in Algorithm 1. The $\Delta \mathrm{L_{A,G}}$ levels, calculated using the array microphones at both receiver heights, are presented in Fig. 9. It can be observed that variations across the noise event are more pronounced at the lower receiver height of 1.75 m. These $\Delta \mathrm{L_{A,G}}$ values are subsequently subtracted from the *Munisense*-measured noise levels (shown as dashed lines in Fig. 10) to approximate free-field conditions. The resulting corrected noise levels are shown as solid curves in Fig. 10, where blue and red denote receiver heights of 1.75 m and 4.5 m, respectively. These corrected levels are then compared to the array-based measurements, represented by the pink dashed curve, which serves as a reference for individual flyover noise comparisons. The improved alignment of the red and blue curves with the reference curve confirms enhanced accuracy under the assumed free-field conditions. And the still remaining difference is attributed to background noise that could not be eliminated.

This analysis was performed for all measured flyovers (three days in Table 1). Although the cumulative effect of

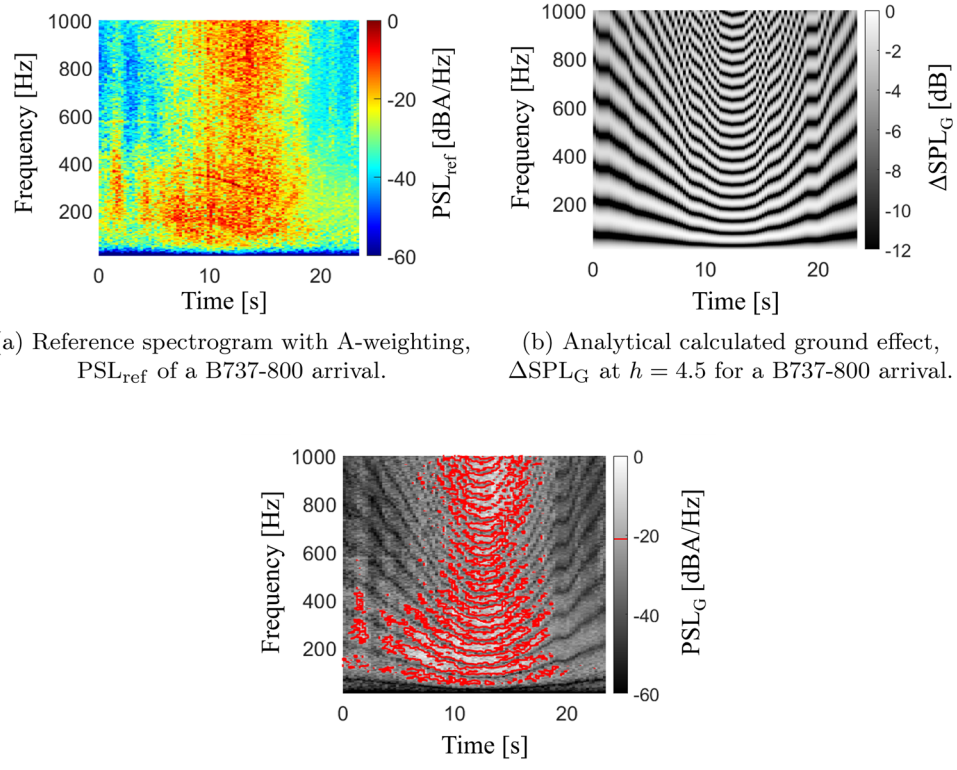


**Fig. 6** Tool-chain for generating a semi-synthetic spectrogram with an exemplary arriving flyover of aircraft type B737-800

(a) Reference spectrogram with A-weighting, $\mathrm{PSL_{ref}}$ of a B737-800 arrival.

(b) Analytical calculated ground effect, $\Delta \mathrm{SPL_G}$ at $h = 4.5$ for a B737-800 arrival.

(c) Semi-synthetic spectrogram obtained after superimposing the reference spectrogram and analytical ground effect, $\mathrm{PSL_G}$ for a B737-800 arrival.

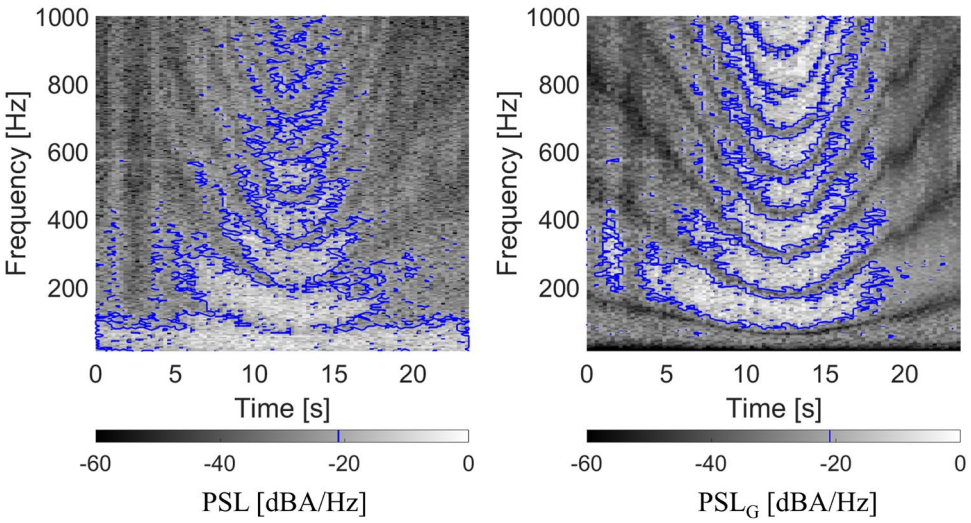


**Fig. 7** Visual comparison between the the *Munisense* measured spectrogram (left) and array obtained semi-synthetic spectrogram at $h = 1.75$ (right) of the exemplary arriving flyover of B737-800

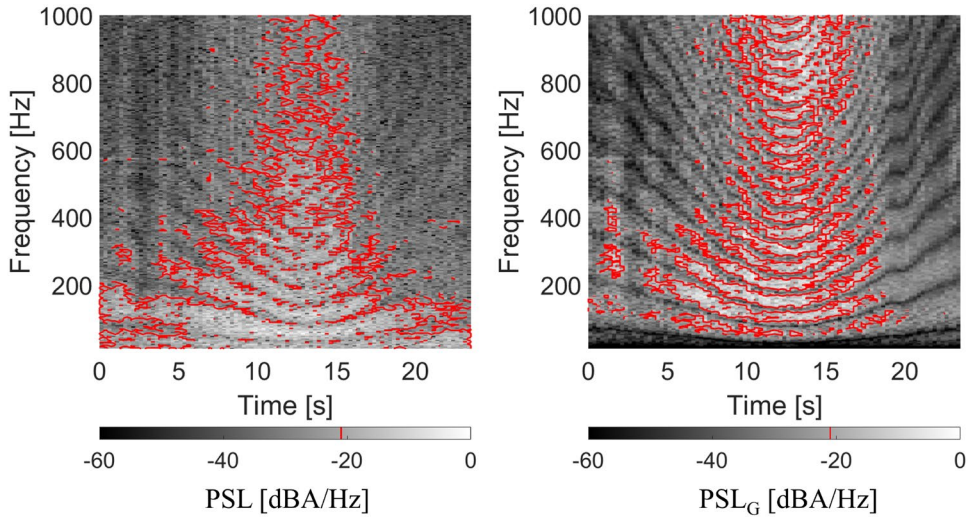


**Fig. 8** Visual comparison between the the *Munisense* measured spectrogram (left) and array obtained semi-synthetic spectrogram at $h = 4.5$ (right) of the exemplary arriving flyover of B737-800

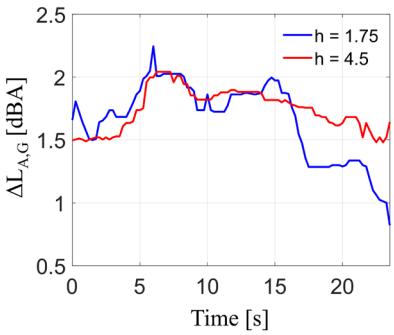


**Fig. 9** Isolated and quantified A-weighted $\Delta L_{A,G}$ obtained from the array microphones for the receiver heights of 1.75 m (blue) and 4.5 m (red) of the exemplary arriving flyover of B737-800

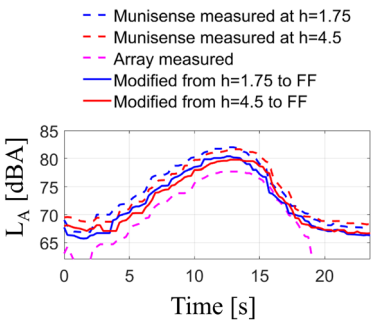


**Fig. 10** *Munisense* measured (dashed) and corresponding ground-effect-corrected noise levels (blocked) obtained at receiver heights of 1.75 m (blue) and 4.5 m (red) of the exemplary arriving flyover of B737-800, where the pink dashed curve is the reference noise curve measured by the microphone array

a noise event is typically assessed using Sound Exposure Level (SEL), some flyovers lacked a sufficient 10 dBA downtime to fulfill this criterion, which can be seen in an exemplary departing flyover shown in Fig. 11. Here, the peak of the noise event in this example is broad and the difference between the maximum and minimum $L_A$ levels is approximately 6 dBA. To address this, an alternative metric is introduced, denoted as $L_{A,max\pm2}$. It represents the arithmetic averaged A-weighted Sound Pressure Level

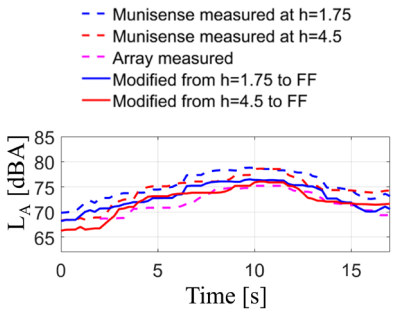


**Fig. 11** *Munisense* measured (dashed) and corresponding ground-effect-corrected noise levels (blocked) obtained at receiver heights of 1.75 m (blue) and 4.5 m (red) of the exemplary departing flyover of B737-800, where the pink dashed curve is the reference noise curve measured by the microphone array

calculated over a 4-second window centered on the $L_{A,max}$ peak (2 s before and after). Since the array serves as reference for all flyovers, $L_{A,max\pm2}$ values are computed for the array-measured curve, both *Munisense* measured curves, and their corresponding ground-effect-corrected versions.

The calculated $L_{A,max\pm2}$ values for all flyovers of the three days are illustrated in Figs. 12, 13, 14. In each figure, the top subplot illustrates the differences in the *Munisense* measured levels, made at $h = 1.75$ and $h = 4.5$, with the corresponding array measurements annotated above their respective bars. In a similar manner, the middle subplot shows the differences between the ground-effect-corrected levels and the array-measured levels. The bottom subplot illustrates the differences between the above two subplots per flyover for both receiver heights, which are denoted as $\Delta(L_{A,max\pm2})$. This metric represents a single value metric of the influence of the ground effect for each flyover.

The flyovers that are observed at low-elevation angles (Day 1 and Day 3) show a mean difference of 1.8 dBA in $\Delta L_{A,max\pm2}$ values. For flyovers observed at higher elevation angles, the mean difference in $\Delta L_{A,max\pm2}$ is 2.3 dBA.

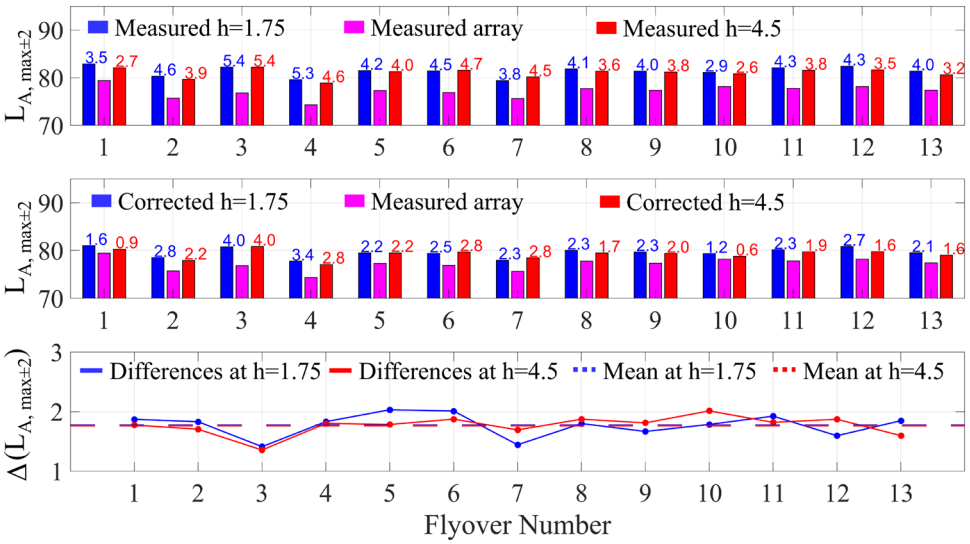


**Fig. 12** Flyovers recorded on Day 1 with $L_{A,max\pm2}$ values obtained from measured curves (top), $L_{A,max\pm2}$ values obtained from ground-effect-corrected curves (middle), and where the differences $\Delta(L_{A,max\pm2})$ with the array values are annotated above the bars and also plotted with their mean values (that overlap in this figure) (bottom)

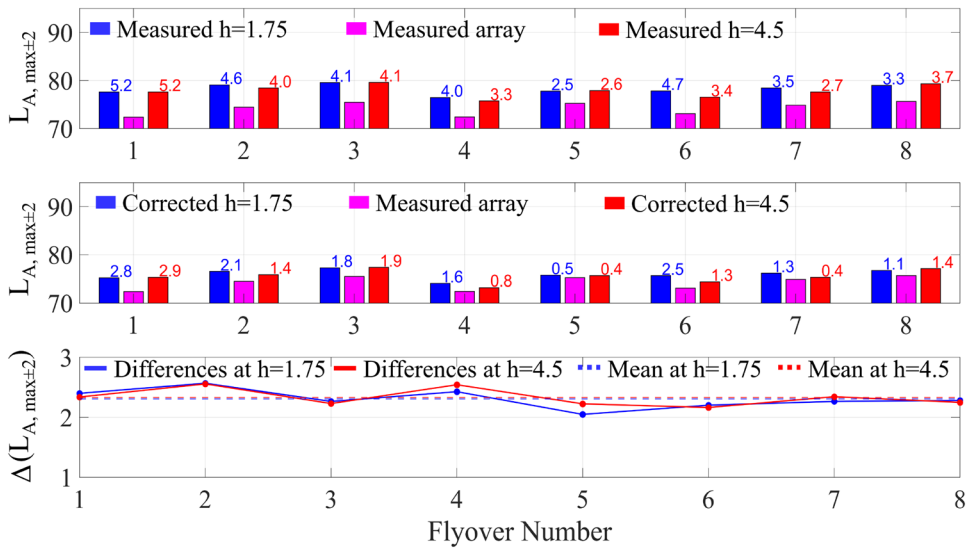


**Fig. 13** Flyovers recorded on Day 2 with $L_{A,max\pm2}$ values obtained from measured curves (top), $L_{A,max\pm2}$ values obtained from ground-effect-corrected curves (middle), and where the differences $\Delta(L_{A,max\pm2})$ with the array values are annotated above the bars and also plotted with their mean values (that overlap in this figure) (bottom)

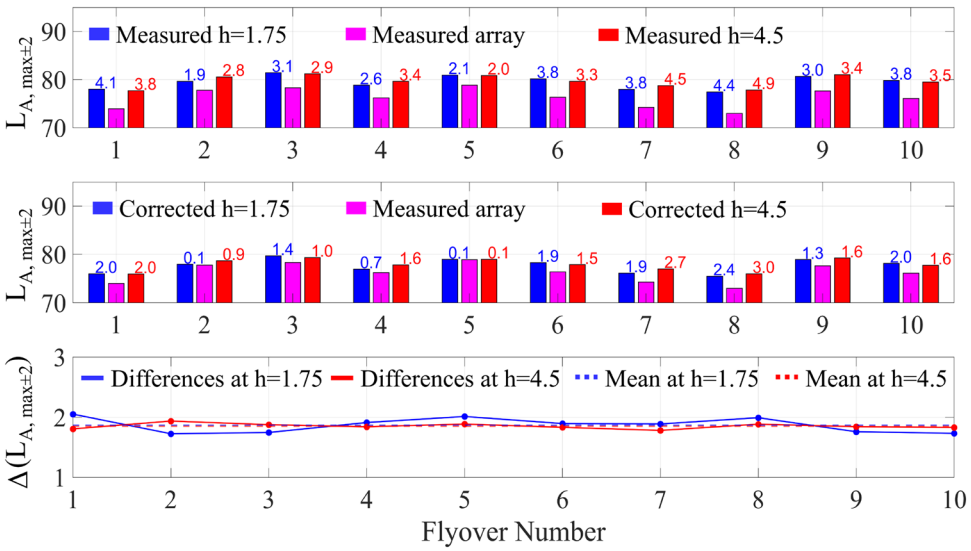


**Fig. 14** Flyovers recorded on Day 3 with $L_{A,max\pm2}$ values obtained from measured curves (top), $L_{A,max\pm2}$ values obtained from ground-effect-corrected curves (middle), and where the differences $\Delta(L_{A,max\pm2})$ with the array values are annotated above the bars and also plotted with their mean values (bottom)

**Table 4** Root-mean-square (RMS) values of measured and ground-effect-correct values with the reference for all flyovers recorded on separate days

| Day | Measured ($h = 1.75$) | Corrected ($h = 1.75$) | Measured ($h = 4.5$) | Corrected ($h = 4.5$) |
|---|---|---|---|---|
| Day 1 | 4.2587 | 2.5325 | 3.9369 | 2.2620 |
| Day 2 | 4.0942 | 1.8535 | 3.7142 | 1.5158 |
| Day 3 | 3.3523 | 1.5878 | 3.5315 | 1.7837 |

Hence, an increase in the ground effect amplification of 0.5 dBA is observed for higher elevation angles than for lower elevation angles. This trend is further supported by a comparison of root-mean-square (RMS) differences between the measured and reference $L_{A,max\pm2}$ values, as well as between the corrected and reference values. The RMS values, calculated across all flyovers recorded over the three days, are summarized in Table 4.

## 5 Conclusions & future work

This paper investigates the propagation phenomenon known as the ground effect, which is prominently observed in noise measurements taken in low-noise regions. The study introduces a measurement-based methodology along with a comprehensive preprocessing toolchain designed to isolate interference patterns caused by the ground effect, using real-life flyover measurements. The novelty of this methodology lies in its use of a phased microphone array as a key instrument towards obtaining a spectrogram devoid of any ground effect by calculating a spatial average of the the pressure signals recorded by all the microphones.

Subsequently the noise levels measured by the single microphone systems (*Munisense*) are corrected to the corresponding free-field conditions. The corrected levels show an improvement in agreement with the ground truth, which are the levels obtained by the array.

A distinct difference between flyovers with low and high-elevation angles is observed through a metric adopted in this paper, i.e., $L_{A,max\pm2}$. The flyovers with low-elevation angles show an average difference of 1.8 dBA and high-elevation angles show an average difference of 2.3 dBA. This finding is different from previous works where it is generally claimed that the ground effect reduces with increasing elevation angles. However, since this dataset does not contain flyovers at grazing angles, it is suggested that more measurements be taken.

Furthermore, it is recommended that future studies investigate the influence of different measurement configurations, such as variations in foam installation, through comparative analysis of reference spectra. Since the analytical approach used in this study is relatively straightforward, extending the analysis to include more complex ray-tracing methods that account for multiple reflecting surfaces would be beneficial.

These insights are crucial for model validation studies, as they highlight the need to consider the influence of measurement configuration on observed levels before comparing model predictions with measurements. Another important application of these findings lies in the modeling itself, where the ground effects also need to be taken into account properly to be able to provide accurate predictions.

**Acknowledgements** Special thanks to the researchers in the Operations and Environment Section (O&E), Amy Morin, Dr. Salil Luesuthiviboon, Rebekka van der Grift & Anique Altena for contributing to the collection of data. The authors are grateful to the EC for supporting the present work, performed within the NEEDED project, funded by the European Union's Horizon Europe research and innovation programme under grant agreement no. 101095754 (NEEDED). This publication solely reflects the authors' view and neither the European Union, nor the funding Agency can be held responsible for the information it contains.

**Author contributions** A.S.J prepared all the figure and tables and wrote the main manuscript. M.S edited the introduction, theory and conclusion sections, A.A.S edited the measurements and results sections. All authors reviewed the manuscript.

**Data availability** No datasets were generated or analysed during the current study.

## Declarations

**Conflict of interest** The authors declare no Conflict of interest.



## References

1. Airbus: Global Market Forecast 2023. Technical report, Toulouse. https://www.airbus.com/en/products-services/commercial-aircraft/market/global-market-forecast
2. World Health Organization(WHO) Europe: Environmental Noise Guidelines for European Region, (2018)
3. European Civil Aviation Conference: ECAC.CEAC Doc.29 4th edition report on standard method of computing noise contours around civil airports volume 1: Applications Guide. Technical report
4. European Civil Aviation Conference: ECAC.CEAC Doc.29 4th Edition, 2016 Report on Standard Method of Computing Noise Contours around Civil Airports Volume 3, Part 1-Reference Cases and Verification Framework. Technical report
5. European Civil Aviation Conference: ECAC.CEAC Doc.29 4th Edition, 2016 Report on Standard Method of Computing Noise Contours around Civil Airports Volume 2: Technical Guide. Technical report
6. Aircraft Noise and Performance: European Union Aviation Safety Agency (2024). https://www.easa.europa.eu/en
7. SAE International: AIR5662: Method for Predicting Lateral Attenuation of Airplane Noise. Technical report (October 2019). https://www.sae.org/standards/content/air5662/
8. Berton, J.J.: Simultaneous use of ground reflection and lateral attenuation noise models. AIAA Aviation and Aeronautics Forum and Exposition, AIAA AVIATION Forum 2021 (2021) https://doi.org/10.2514/6.2021-2214
9. Walker, D.Q.: An analysis of aircraft flyover noise. Technical report, Aerospace medical research laboratory, Canoga Park (April 1978). https://apps.dtic.mil/sti/citations/ADA058522
10. Chessell, C.I.: Propagation of noise along a finite impedance boundary. J. Acoust. Soc. Am. **62**(4), 825–834 (1977). https://doi.org/10.1121/1.381603
11. Delany, M.E., Bazley, E.N.: Monopole radiation in the presence of an absorbing plane. J. Sound Vib. **13**(3), 269–279 (1970). https://doi.org/10.1016/S0022-460X(70)80019-0
12. Embleton, T.F.W., Piercy, J.E., Daigle, G.A.: Effective flow resistivity of ground surfaces determined by acoustical measurements. J. Acoust. Soc. Am. **74**(4), 1239–1244 (1983). https://doi.org/10.1121/1.390029
13. Kayser, B., Dragna, D., Blanc-Benon, P.: Heuristic solution for the acoustic radiation of a moving monopole in an inhomogeneous and moving atmosphere. Appl. Aircr. Noise. Acta Acust. **8**, 62 (2024). https://doi.org/10.1051/aacus/2024048
14. Albert, M., Bousquet, P., Lizarazu, D.: Ground effects for aircraft noise certification. In: 23rd AIAA/CEAS Aeroacoustics Conference, 2017, p.3845 . American Institute of Aeronautics and Astronautics Inc, AIAA, Denver (2017). https://doi.org/10.2514/6.2017-3845
15. Bousquet, P., Blandeau, V.: Feasibility of determining aircraft certification noise levels using ground plane microphone measurements. In: AIAA Aviation and Aeronautics Forum and Exposition, AIAA AVIATION Forum 2021, p. 2159. American Institute of Aeronautics and Astronautics Inc, AIAA, Virtual event. (2021). https://doi.org/10.2514/6.2021-2159
16. Giannakis, J.M., Nesbitt, E.H.: Evaluation of a correction factor for flyover-noise ground plane microphones. In: AIAA AVIATION 2020 FORUM, p. 2612 . American Institute of Aeronautics and Astronautics Inc, AIAA, Virtual event (2020). https://doi.org/10.2514/6.2020-2612
17. Go,S., Kingan, M.J., Schmid, G., Hall, A. : On the use of groundboard mounted microphones for outdoor noise measurement, J. Sound and Vibrations, **584, 118432** (2024). https://doi.org/10.1016/j.jsv.2024.118432
18. polySound: Akotherm Basic 40/25. chrome-extension://efaidnbmnnnibpcajpcglclefindmkaj/https://www.polygroup.nl/wp-content/uploads/2017/03/1.-Akotherm-Basic.pdf
19. Flamex Basic. chrome-extension://efaidnbmnnnibpcajpcglclefindmkaj/https://media.pim.merford.com/uploads/pdf/1/3/131_flamex-basic.pdf
20. Merino-Martínez, R., Sijtsma, P., Snellen, M., Ahlefeldt, T., Antoni, J., Bahr, C.J., Blacodon, D., Ernst, D., Finez, A., Funke, S., Geyer, T.F., Haxter, S., Herold, G., Huang, X., Humphreys, W.M., Leclère, Q., Malgoezar, A., Michel, U., Padois, T., Pereira, A., Picard, C., Sarradj, E., Siller, H., Simons, D.G., Spehr, C.: A review of acoustic imaging methods using phased microphone arrays: Part of the Aircraft Noise Generation and Assessment Special Issue. CEAS Aeronautical Journal **10**(1), 197–230 (2019) https://doi.org/10.1007/s13272-019-00383-4
21. Jayanthi, A.S., Snellen, M., Amiri-Simkooei, A.R., Sijtsma, P., Van Oosten, N.: A comparison of source localization methods with varying sizes of the phased microphone array. In: Berlin Beamforming Conference, Berlin, pp. 1–10 (2024). https://pure.tudelft.nl/ws/portalfiles/portal/217205867/BeBeC_2024_Conference_Paper_1_.pdf
22. Olive, X., Krummer, J., Figuet, B., Alligier, R.: Filtering Techniques for ADS-B Trajectory Preprocessing. Journal of Open Aviation Science **2**(2) (2025) https://doi.org/10.59490/joas.2024.7882
23. Attenborough, K., Taherzadeh, S.: Prediction of outdoor ground effect. Applied Acoustics **242** (2026) https://doi.org/10.1016/j.apacoust.2025.111067
24. Arntzen, M., Simons, D.G.: Modeling and synthesis of aircraft flyover noise. Appl. Acoust. **84**, 99–106 (2014). https://doi.org/10.1016/j.apacoust.2013.09.002
25. Delany, M.E., Bazley, E.N.: Acoustical Properties of Fibrous Absorbent Materials. Technical report, National Physical Laboratory, Middlesex (August (1969)